Effect of aggregate shapes on local fields in 3D mesoscale simulations of the concrete creep behavior

Fabien Bernachy-Barbe, Benoît Bary

Finite Elements in Analysis and Design 156 (2019) 13–23

Contents lists available at ScienceDirect

Finite Elements in Analysis and Design

journal homepage: www.elsevier.com/locate/finel

Effect of aggregate shapes on local fields in 3D mesoscale simulations of the concrete creep behavior

Fabien Bernachy-Barbe *, Benoît Bary

Den-Service d'Etude du Comportement des Radionucléides (SECR), CEA, Université Paris-Saclay, F-91191, Gif-sur-Yvette, France

ARTICLE INFO

Keywords:
Concrete
Creep
3D numerical simulation
FEM
FFT-Based methods
Viscoelasticity
Viscoplasticity

ABSTRACT

Describing accurately the creep behavior of concrete is of significant importance for the evaluation of the long-term performance of structures. In this regard, a finer characterization of mesostructure effects and material non-linearity provides very insightful information. In this work, the effects of aggregate shapes on the creep response are studied using numerical simulations on 3D mesoscopic samples. The main focus is put on the assessment of the representativeness of generated samples versus real specimens obtained by tomography. Several mesostructures are generated by randomly distributing aggregates with different geometries, from simple spheres to realistic ones extracted from tomography. Creep simulations with finite element (FE) and Fast Fourier Transform (FFT) methods are then performed on different spatial refinements. Moreover, a classical linear viscoelastic (VE) and a viscoelastic-viscoplastic (VE-VP) behavior able to reproduce non-recoverable strains are adopted for describing the matrix behavior, to assess the relevance of a more accurate model. It is shown that numerical samples generated with tomographic aggregates may be regarded as a good approximation of the real specimen, while more 'isotropic' shapes, especially spherical, lead to significant differences at both local and macroscopic levels. Results obtained with FE and FFT methods are very close, indicating that while FFT is well adapted, FE remains attractive in this context. Finally, notable differences are observed between VE and VP response due to the development of residual strains in the matrix and correspondingly more limited strain redistribution, which indicates that VP-like models should be preferred to capture accurately the creep features at mesoscale.

1. Introduction

Concrete structures designed in the context of nuclear activities (in particular containment buildings and waste storage structures) have generally to fulfill high levels of containment and protection against radionuclide migration. The performance and durability of the material is then of crucial importance. Long-term creep and induced development of cracks are well known phenomena leading to a reduction of containment capabilities. Therefore its accurate characterization and modelling contribute to a better description and prediction of the concrete behavior and structure response.

At mesoscale, concrete is a heterogeneous material that may be described at first glance by linear elastic aggregates distributed in a mortar matrix ruled by a time-dependent behavior and concentrating the viscoelastic mechanisms. Great efforts have been made in the past two decades to estimate and analyze the mechanical and creep response of concrete by explicitly accounting for its main constitutive phases. To this aim, analytical homogenization techniques can be applied to the composite (including in some cases aggregate/matrix interfaces) to obtain approximations of the macroscopic mechanical effective properties, see e.g. Refs. [1–3]. However such methods, although versatile and relatively easy to manipulate, suffer generally from a simple mesostructure representation, in particular when the aggregate shapes are irregular and non-convex. Besides, classical mean-field homogenization techniques are approximate by nature, and the estimations deviate increasingly from the 'real' sought properties when the volume fraction of the inclusive phases or properties contrast are high. Furthermore, they do not permit in general to obtain accurate information on the local response of the materials, which are complex to capture especially when nonlinearities are considered. Such analyses of the local fields can, however, provide insight into both stress and strain redistribution mechanisms occurring for non-linear mechanical behaviors, and for microcracking description. On the other hand, 3D computational analysis represent an alternative and promising way of capturing overall as well as local response of

* Corresponding author.
E-mail address: fabien.bernachy-barbe@cea.fr (F. Bernachy-Barbe).

https://doi.org/10.1016/j.finel.2019.01.001
Received 26 September 2018; Received in revised form 3 January 2019; Accepted 4 January 2019
Available online 21 January 2019

specimens, either numerically generated or experimentally obtained. Following the increasing power of computers, they are more and more used on numerical samples whose description and representation are growingly accurate and realistic. Besides the classical finite element method (FEM) to solve the problem, alternative techniques have emerged as the FFT-based method to reduce the shortcomings of computational costs and tricky meshing procedures (e.g. Refs. [4,5]). Regarding concrete, these procedures have been successfully applied to analyze for instance the effects of aggregate shapes and aggregate/matrix interfaces (e.g. Refs. [6–8]), or the initiation and propagation of cracks ([9–11]) on numerically generated samples having different configurations. In parallel, X-ray Computed Tomography have allowed obtaining extremely accurate descriptions of the mesostructure (the fineness of the details is only limited by the image resolution), which makes it possible to examine the response of much more representative and complex specimens (see e.g. Refs. [12,13]). Note that while such experimentally obtained samples characterize almost perfectly the real material, generated mesostructures have the advantage to allow examining the effect of some parameters that are impossible in practice to control independently with experimental specimens, as the mineralogical nature (and their mechanical properties), size, shape, spatial distribution etc. of aggregates or inclusions. In this sense, the numerical procedures, once validated, give the possibility to perform 'virtual tests' in a much easier way than real experiments. On the other hand, the question of the representativeness of these fully generated mesostructures arises, and it is in general relatively difficult to precisely evaluate it.

In this study, we investigate the mesoscopic response of numerically generated samples of concrete assumed to be composed of a homogeneous viscoelastic mortar matrix in which are distributed elastic aggregates of various size and shape subjected to creep loadings. Experimental data on corresponding mesostructures are not available (and would be hardly feasible), so that the comparative analysis is made on a purely numerical basis. As it is not the focus of the paper, we also suppose that all complex micromechanisms affecting creep in the cement paste can be described at the mortar scale through a simple viscoelastic (possibly coupled with plasticity) approach. The detailed effects of e.g. relative humidity and temperature on creep phenomena are beyond the scope of the study. Another simplifying hypothesis is that the interfaces between matrix and aggregates are considered as perfectly bonded, as at the mesoscale their influence is reported to be weak (see e.g. Refs. [8,14]). Note that such hypothesis is no longer valid for mortar materials, i.e. at microscale, since in this case the ITZ size could not be ignored with respect to the aggregate dimensions (sand grains sizes range between several hundreds of micrometers to several millimeters, while typical ITZ size is around 20 μm), and correspondingly their impact becomes non-negligible. It is also assumed that the material is not subjected to damage, a hypothesis that experimental data justifies in a regime of basic creep and moderate loadings. Loading rates of 20%–40% of the material strength in compression were repeatedly shown to induce little to no damage as indicated through the linearity of the creep behavior and constancy of the Poisson's ratio (and absence of dilatant effects) [15] and from acoustic emission measurements [16].

The main objective of the paper is then to examine and assess the suitability of the obtained virtual samples and their construction methodology to reproduce the behavior of real concretes, which is an important aspect related to numerical generation procedures. Accordingly, a special attention is paid to the effects of aggregate shapes on both overall and local response. A related question is to quantify the level of accuracy provided by different shapes of aggregates, from very simple (sphere) to more complex ones (polyhedrons), up to 'real' tomographic aggregates. To achieve this analysis, we propose to generate several samples of virtual concrete with different aggregate shapes while keeping the same volume fraction and size distribution, and to compare the results with those obtained with a real tomographic sample. Another point is to study the effects of two different approaches to describe the creep behavior, i.e. a linear viscoelastic model and a richer viscoelastic-viscoplastic one. The main difference between these two models lies in the ability of the latter to reproduce irrecoverable strains appearing after unloading, that may be expected to be of importance for complex loading paths and the prediction of damage. Although numerical mesoscale approaches to concrete creep are commonly using linear viscoelastic models [7], mechanisms specific to viscoplasticity such as in Ref. [17] deserve further study. This aspect is interesting regarding the lower computational costs and much simpler micromechanical analytical treatment of the linear viscoelastic behavior. Finally, the simulations will be performed with two numerical methods, namely the classical FEM and the FFT-based method. The latter is deemed to be of greater efficiency for solving problems on numerical periodic samples, while the former is more versatile and can be applied on any types of structures. An interesting aspect is then to assess the degree of accuracy and effectiveness of these methods for viscoelastic problems on heterogeneous mesostructures. The effects of the mesh fineness and grid resolution, and boundary conditions for FEM, will also be studied.

The results obtained will be compared in terms of macroscopic strain, per phase average strains and stresses evolutions, and stresses distribution in both phases in the case of a creep loading followed by recovery. The distribution of a damage-like variable will also be investigated through an index calculated from the local positive strains at the post-processing stage.

2. Models and methods

2.1. Linear viscoelasticity and viscoelastic-viscoplastic model for creep

The models used in this study for reproducing the matrix behavior are briefly described in this section. Note that the viscoplastic model is constructed from the viscoelastic one by introducing additional terms for expressing the viscoplastic strains. By this way, the same numerical implementation serves for both linear viscoelastic and viscoplastic simulations, the former case obtained by simply disregarding the viscoplastic strains. As mentioned above, the aggregates are assumed isotropic linear elastic, with Young modulus and Poisson coefficient equal to 70 GPa and 0.3, respectively.

Linear viscoelasticity is expressed in a stress-based formulation as:

$$\underline{\underline{\varepsilon^{ve}}} = \boldsymbol{S}^0 : \underline{\sigma} + \int_0^t \Delta\boldsymbol{S}(t-\tau) : \underline{\sigma}(\tau) d\tau \tag{1}$$

$$\Delta\boldsymbol{S}(t) = \sum_{n=1}^{N} \boldsymbol{S}^n \lambda_n \exp(-\lambda_n t) \tag{2}$$

with λ_n the inverse characteristic times, $\boldsymbol{S}^0$ the instantaneous compliance tensor and $\boldsymbol{S}^n$ the delayed compliance tensors (which are assumed isotropic and described in the following through their inverse, using the corresponding Young's modulus E_n and Poisson's coefficient ν_{ve}). Three time scales are considered in the present model ($N = 3$) considering three temporal decades of interest in the applied loadings (1, 10, 100 days).

A large part of the basic creep strains in cementitious materials is not recoverable (in particular long-term creep, and independently of ageing). Some proposed mechanisms include sliding of C—S—H sheets, water microdiffusion and/or microcracking (e.g. Refs. [16,18,19]). In order to take into account these irrecoverable strains, we propose to introduce a purely viscoplastic part in the formulation. A non-linear viscoelastic-viscoplastic (VE-VP) model is then built by writing the following simple strain decomposition, in a way similar to Darabi [20], itself a particular model derived from the general Schapery models [21]:

$$\underline{\underline{\varepsilon^{vevp}}} = \underline{\underline{\varepsilon^{ve}}} + \underline{\underline{\varepsilon^{vp}}} \tag{3}$$

The viscoplastic model is taken of the Perzyna form:

$$\underline{\underline{\dot{\varepsilon}^{vp}}} = \Gamma\phi\frac{\partial\phi}{\partial\underline{\underline{\sigma}}} = \dot{p}\underline{\underline{n}} \tag{4}$$

with Γ the viscoplastic fluidity parameter, ϕ the yield function and ϕ its positive part; it is expressed with p the cumulated plastic strain and $\underline{\underline{n}}$ the flow direction tensor. A simple yield function with linear hardening is taken for the purpose of the present work; it is expressed as:

$$\phi = \left(\sqrt{J_2 + MI_1^2} - \sigma_y\right) - Hp \tag{5}$$

with I_1 the first stress invariant, J_2 the second invariant of the deviatoric part of the stress tensor and σ_y, H and M material constants corresponding respectively to the yield stress, the hardening modulus and M a parameter linked to the irrecoverable creep "Poisson's coefficient".

Both models have been calibrated based on a short term creep-recovery test on cement paste by Parrott [22] due to its good quality of transverse strain measurement; it yields directly the instantaneous elastic properties as $E = 14\ GPa$, $\nu = 0.242$. The viscoelastic model has been identified only on the creep phase while the VE-VP model is identified on the whole strain response (see Fig. 1). The model parameters are given in Table 1. Considering that only one test at a single stress level is available, the identification is underdetermined. It is postulated for the present example that $\sigma_y = 5\ MPa$ corresponding to the assumption that creep is fully recoverable for approximately 15% of the compressive strength. That hypothesis is sufficient to identify with a least squares procedure the viscoelastic parameters on the recovery branch and then the combined VE-VP parameters on the creep branch. Although results may differ quantitatively, most of the following conclusions hold for any reasonable non-zero value of the yield stress.

This model was finally formulated as a non-linear system of partial differential equations, following in particular Crochon [23] for the integration of the viscoelastic part. This constitutive model was implemented using the MFront tool (http://tfel.sourceforge.net/), which allowed to automatically generate an efficient implicit integration procedure usable by both our FFT and FE solvers [24].

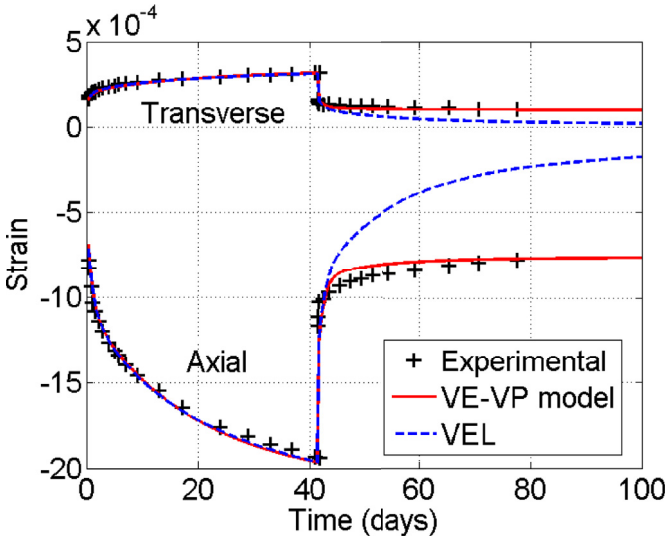

Fig. 1. Identification of the constitutive models.

Table 1
Material parameters identified for the constitutive models.

Param.	*VE-VP*	*VE*
λ_1, E_1	*1* d^{-1}, 20 GPa	*1* d^{-1}, *20.*5 GPa
λ_2, E_2	*0.1* d^{-1}, 85 GPa	*0.08* d^{-1}, *14.*5 GPa
λ_3, E_3	*0.01* d^{-1}, 100 GPa	*0.01* d^{-1}, 10 GPa
ν_{ve}	*0.11*	*0.12*
Γ	*7.10*$^{-6}$ $d^{-1}MPa^{-1}$	-
σ_y	5 MPa	-
H	7 GPa	-
M	*0.325*	-

2.2. FFT-based and finite element-based integration of mechanical boundary value problems

As mentioned in the Introduction, one objective of the study is to test and apply FE and FFT-based numerical methods to solve the problem on the heterogeneous mesostructures. The interest is to evaluate the level of accuracy of both methods and their respective adequacy in the case of complex mesostructures with non-linear viscoelastic-viscoplastic behavior. In theory FFT-based solvers are more efficient for the heterogeneous mesostructures considered in this study, while FEM is more flexible and can be used for any morphology and structure type (not only Representative Volume Elements, RVE). However it suffers generally from a higher computational cost and requires a tricky meshing procedure when unstructured meshes are involved (see e.g. Ref. [4]).

The FE code Cast3M (http://www-cast3m.cea.fr/) developed at the French Atomic Energy Commission (CEA) is used to perform the FE simulations. The direct solver is applied along with the modified Newton-Raphson method, associated with a convergence acceleration procedure which takes advantage of the three previous iteration results to estimate the new strain increment.

FFT-based methods [25] allow solving numerically in an efficient manner the problem of a heterogeneous unit-cell submitted to periodic boundary conditions. In linear elasticity, and under imposed strains, the mechanical problem can be formulated as:

$$\begin{cases} div(\underline{\underline{\sigma}}(x)) = 0 \\ \underline{\underline{\sigma}}(x) = C(x) : \underline{\underline{\varepsilon}}(x) \\ u(x) = \underline{\underline{E}}.x + u^*(x) \\ u^*(x)\ periodic\ on\ opposite\ boundaries \\ \underline{\underline{\sigma}}.n\ antiperiodic\ on\ opposite\ boundaries \end{cases} \tag{6}$$

with $\boldsymbol{C}(x)$ the stiffness tensor at each point of the unit-cell, $\underline{\underline{E}}$ the imposed macroscopic strains and $u^*(x)$ the fluctuations of the displacement field. This problem can be rewritten with the introduction of a homogeneous reference medium of stiffness tensor $\boldsymbol{C}^0$ (Lippmann-Schwinger equation):

$$\underline{\underline{\varepsilon}}(x) = -\left(\boldsymbol{\Gamma}^0 * \underline{\underline{\tau}}\right)(x) + \underline{\underline{E}} \tag{7}$$

$$\underline{\underline{\tau}}(x) = \left(\boldsymbol{C}(x) - \boldsymbol{C}^0\right) : \underline{\underline{\varepsilon}}(x) \tag{8}$$

with $\boldsymbol{\Gamma}^0$ the periodic Green operator associated to the reference medium $\boldsymbol{C}^0$ and $*$ representing the convolution product. The principle of solving this problem using FFT-based methods can be summarized as follows: first the polarization field $\underline{\underline{\tau}}$ is evaluated at each point x of the grid, then the discrete (Fast) Fourier Transform (FFT) of this field is performed in order to compute effectively the convolution product, and finally the inverse Fourier transform is computed to obtain $\underline{\underline{\varepsilon}}(x)$ in the real space. In the case of non-linear behaviors considered here, the stiffness $\boldsymbol{C}(x)$ is straightforwardly replaced by the adequate tangent operator $\boldsymbol{C}^*(x)$ (linearized problem) [26]. In the used FFT solver, AMITEX_FFTP [27] (http://www.maisondelasimulation.fr/projects/amitex/html/) the convergence acceleration technique used in FE code Cast3M is applied advantageously to the classical fixed-point algorithm. For the problem under consideration, these methods have strong benefits relatively to finite element (FE) methods who suffer, as already mentioned above, from a high numerical cost. The mesostructure being represented as a 3D regular array of points (seen as "voxels"), the meshing step required for FE, which may be tricky especially if periodicity of the samples is required, is avoided entirely. It is therefore possible to perform direct simulations on experimental geometries obtained from imaging (2D) and

tomography (3D). At last, these methods are easily parallelized and allow dealing with complex mechanical behaviors on fine grids with reasonable computation times.

2.3. Mesostructure generation

The direct use of mesostructures obtained from tomographic images for FFT computations is problematic because they are generally non-periodic and edge effects arise due to "cut" features at the boundaries. In order to get realistic mesostructures, it is proposed to extract real aggregates from a tomographic image, measure their properties (the size distribution here, but more refined methods can be conceived), and generate a periodic RVE with such properties using the extracted aggregate shapes. Note that alternative efficient approaches exist to create numerically accurate random aggregate shapes, as for instance by using spherical harmonic series combined with X-ray computed micro-tomography (see Refs. [28,29]).

In practice, aggregates were obtained from the X-ray Computed Tomography (X-CT) of a diameter 110 mm cylindrical concrete sample, obtained at BAM (Berlin, Germany), that was cropped to a cubic box of size approximately 75 mm and resampled (using trilinear interpolation) to be of size 511^3 voxels (Fig. 2 a.). After standard Gaussian filtering and beam-hardening correction, this image was then segmented with a simple threshold on the grey levels. A series of morphological operations (opening and closing) allowed to eliminate all aggregates of equivalent radius equal or below 7 voxels (they are counted as matrix) while eliminating holes inside the aggregates and preserving as accurately as possible their shapes (Fig. 2 b.), in a way similar to Ref. [12]. A limitation of such image processing techniques is the loss of some geometrical features under the size of the structuring element (here a ball of radius 3 voxels, which corresponds to a physical size of approximately 0.44 mm). This mesostructure were used directly to perform FFT simulations (Fig. 3 g.). Aggregates were individually isolated by detecting the contiguous regions obtained after a morphological erosion (to avoid counting touching aggregates as one), eliminating aggregates cut at the edges of the domain (which may create some bias). They were restored back to their initial (approximate) geometry by performing the opposite morphological dilation (Fig. 2 c.). They were then measured: the resulting size distribution that was used for the last steps of the generation procedure is presented in Fig. 4; the total aggregate volume fraction is 39.83%. Note that typically in standard concrete such concentration is close to the one of coarse aggregates (i.e. gravel), while the total volume fraction of particles including sand grains ranges generally between 65 and 70%. Considering around 40% of volume fraction of aggregates dispersed in a mortar matrix appears then justified. Finally, the biggest 100 aggregates' surfaces were first finely meshed and their meshes were coarsened to be of the order of 100–200 triangles for the meshes to be of reasonable size, and stored as a library of ".stl" meshes (Fig. 2 d.).

The procedure for generating the mesostructure geometries and subsequent meshes and "voxellized" images is detailed in Ref. [30]. It has been applied to various problems relative to the concrete behavior at mesoscale, including drying and carbonation [31], corrosion [32] and analysis of matrix/aggregate interface effects [8]. It relies on the open-source python library Combs implemented in the Computer-Aided

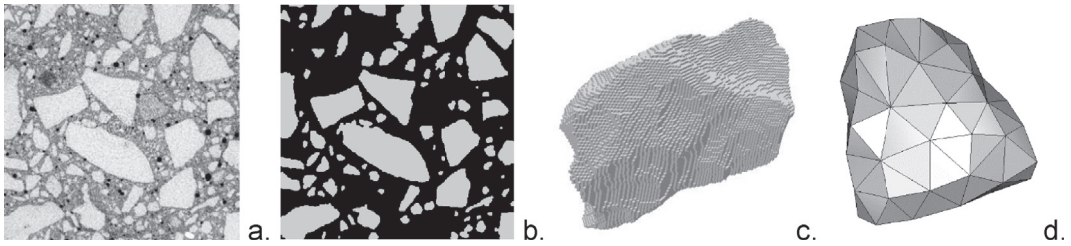

Fig. 2. Illustration of the generation procedure for the aggregate meshes (a. raw X-CT data, b. filtering and segmentation, c. voxel single aggregate extraction and measurement, d. meshing of a simplified geometry).

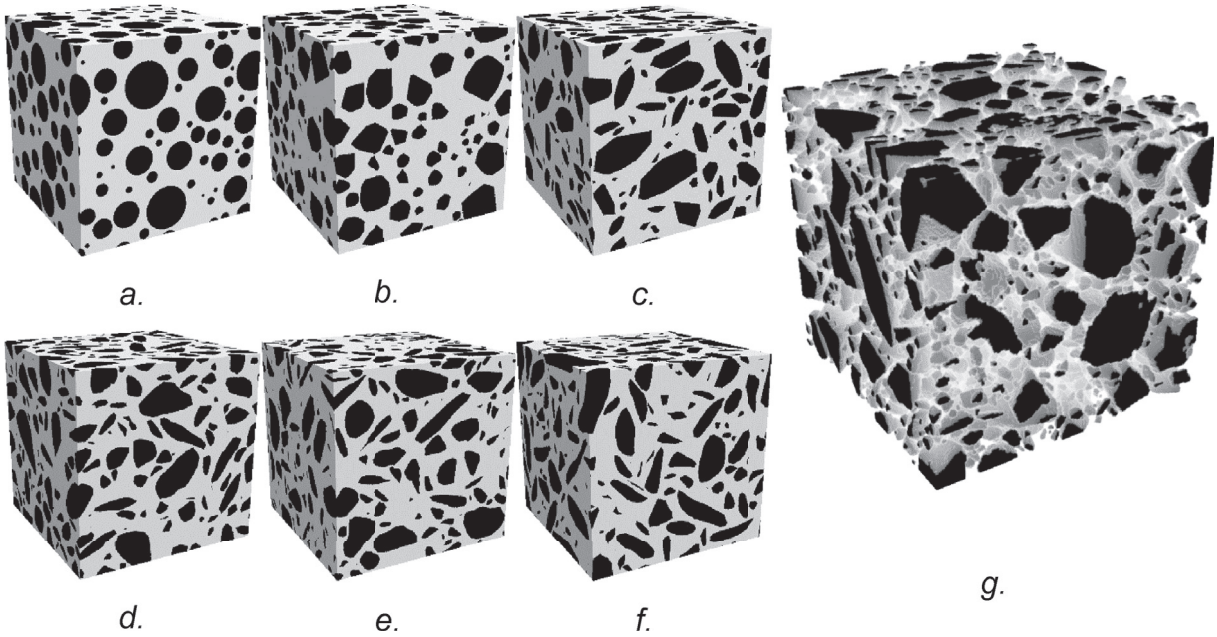

Fig. 3. Five different mesostructure types (a. spheres, b. isotropic Voronoi polyedra, c. flattened Voronoi polyedra, d. e. and f. three "virtual concrete" samples generated using tomographic aggregates, g. 3D view of the non-periodic segmented tomography used for direct FFT computations).

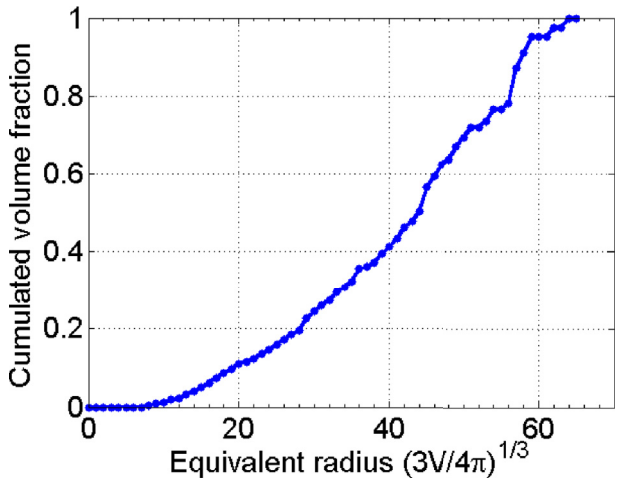

Fig. 4. Experimental sieve curve of aggregates measured using tomography, and used for virtual sample generation (bin size of 1, radius expressed in voxels).

Design code Salome (http://www.salome-platform.org) to produce both geometry and meshes of the mesostructures. As mentioned, the influence of the inclusions shape was studied through samples generated with different aggregates: spheres, polyhedral convex aggregates obtained by a classical Voronoi space decomposition, and the tomographic aggregates described above (see Fig. 3). Further, another shape class was obtained by modifying the initial Voronoi aggregates into flattened inclusions: an aspect ratio of 4 was applied to all shapes along an axis randomly defined before being placed. The corresponding particle shapes were termed as 'anisotropic Voronoi' in the following. As indicated, the aggregate volume fraction was imposed to the same value of 39.83% for all samples. To assess the representativeness of the obtained samples, three realizations were made for each aggregate shape.

The geometries were obtained by randomly distributing in a box the aggregates of prescribed sizes and shapes. More precisely, the placement of aggregates resulted from a random process where points defining the gravity centers were arbitrarily determined in the box, and tests were performed for verifying that the newly placed aggregates did not overlap the already present. The placement procedure has been efficiently improved for the convex aggregates by implementing the GJK [33] 3D algorithm into Combs, which allowed to significantly reduce the computation time of the particle to particle distances (see e.g. http://www. dyn4j.org/2010/04/gjk-distance-closest-points). The periodicity of the numerical samples were further imposed to meet FFT computation requirements, and also to allow applying periodic boundary conditions in FE simulations. Note that similar placement procedures have been applied for generating concrete specimens with realistic aggregate shapes, see e.g. Refs. [28,34]. The unstructured periodic meshes were generated with **triangular** elements for surfaces (MeshGems-CADSurf) and tetrahedral elements for volumes (MeshGems-Tetra) by making use of the automatic meshing softwares developed by Distene (http://www.meshgems.com). The number of linear tetrahedral elements in the reference meshes (see the next section for a study on the effect of the mesh refinement) ranged from 2.45×10^6 to 2.58×10^6 for the polyhedral aggregates and from 2.86×10^6 to 2.9×10^6 for the spherical shapes. All mesostructures were generated following the same size distribution obtained from the tomography to eliminate this factor from the present parametric study (Fig. 4).

3. Results

We present and analyze in this section the results obtained with the different configurations of aggregate shapes, numerical methods and matrix behaviors as considered in this study. The load as used in the model calibration (Fig. 1) is a constant uniaxial stress (creep) $\sigma_{11} = -8,91$ MPa applied during 42 days followed by zero stress for 48 days, discretized in 33 time steps for all the simulations.

3.1. Numerical aspects of the problem

3.1.1. FE boundary conditions

It is well known that the response of numerical samples which are not true RVE depends on the applied boundary conditions (BC) (see e.g. Refs. [4,35]). To evaluate the BC effects on the macroscopic behavior, we analyze the FE response obtained on a particular sample with 3 classical BC types: homogeneous strains (Kinematic Uniform Boundary Conditions - KUBC), homogeneous stresses (Stress Uniform Boundary Conditions - SUBC) and periodic BC (PBC) [35,36]. KUBC are applied by imposing to the nodes belonging to the sample surfaces displacements corresponding to a homogeneous macroscopic strain by appropriate relations, while the external load is prescribed to be the creep stress. Likewise, PBC are set through node-to-node displacement constraints imposed between the two nodes located on the exact opposite positions on the sample faces. Obviously, such BC are possible due to the periodic characteristics of the generated meshes. In this case the FE problem size to solve is significantly greater since these imposed relative displacements are integrated in the matrix of the system as constrained relations.

The Fig. 5 shows the results in terms of macroscopic strains obtained with a Voronoi mesostructure with the 3 different BC (note that for the other shapes the results are analogous). We observe that SUBC and PBC give close results, as already reported in Ref. [8] for similar materials, whereas the response with KUBC differs much more; a strong discrepancy between SUBC and KUBC simulations is then exhibited. We may anticipate from the results in linear elasticity in Ref. [37] that SUBC provides more accurate results than KUBC when the matrix is more compliant than the aggregate phase (this is the reverse when the matrix is stiffer). Moreover, PBC are generally considered as a good compromise and provide precise results with respect to the sought mechanical properties (e.g. Refs. [35,37]). As the computation time with PBC is almost twice the one with SUBC, and given that both results are comparable, in the following the FE simulations are analyzed only through SUBC.

3.1.2. Mesostructure discretization

We examine in this subsection the effect of the mesostructure spatial discretization for the two numerical methods. Three different grid resolutions (127^3, 255^3, 511^3 voxels – odd sizes are faster in the used implementation) for FFT calculations and three different mesh sizes (0.96, 2.49 and 5.02×10^6 elements) for FE simulations are compared. Fig. 6 illustrates the refinement effects by showing a detail of the FE

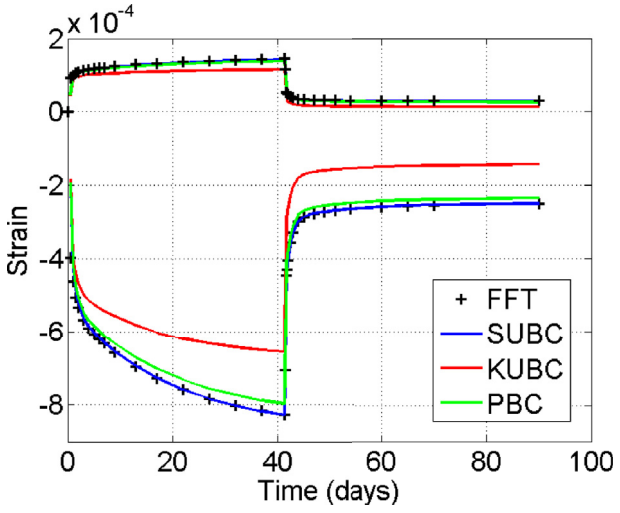

Fig. 5. Macroscopic strains as a function of time for a Voronoi "virtual concrete" with different boundary conditions.

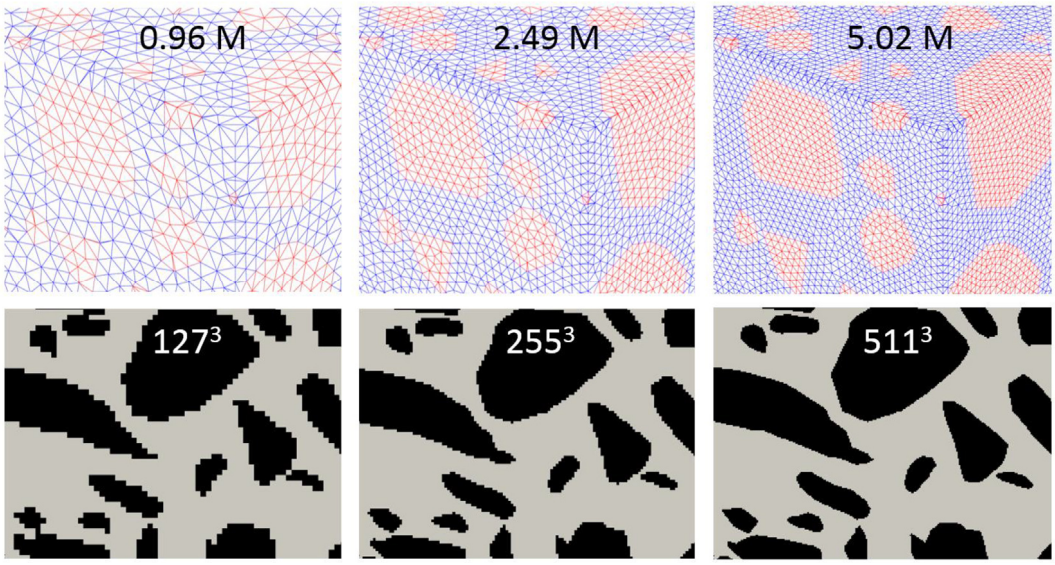

Fig. 6. Top: details of three discretisations of a FE mesh with Voronoi isotropic polyedra (with the number of linear tetrahedral elements) and bottom: three discretisations of a FFT grid with realistic concrete aggregates (with voxel count).

meshes (top) and of the grids (bottom) for the three sizes. The results in terms of axial (i.e., in the direction of the creep loading) macroscopic creep strain as a function of time are plotted in Fig. 7 a) for the FFT calculations on the three virtual concrete mesostructures, and in Fig. 7 b) for the FE simulations on a Voronoi aggregate mesostructure. Overall, we observe the same effect of the refinement for the two computational methods: refining the mesh leads to a slightly more compliant material. It appears that in both cases the response is still slightly different for the two higher refinements, indicating that, in theory, the discretization fineness is not quite sufficient to consider the solutions as totally 'converged'. However as the difference is very limited and the curves comparable, the accuracy can be reasonably regarded as good. In the following, the reference resolution will be 511^3 voxels for the FFT, while the reference number of elements in the FE meshes will range between 2.45×10^6 and 2.9×10^6 elements as explained above.

Concerning the representativeness of the generated samples, it can be seen in Fig. 7 a) that the curves obtained for the three realizations of the virtual concrete and for each grid resolution considered are very close. This means that, at least for the macroscopic results examined here, the mesostructures may reasonably be viewed as representative volume elements. Note that for clarity reason, the FE results obtained with the three realizations of the Voronoi samples are not shown, as they are very similar to the ones provided with FFT calculations.

The computation time for solving the system on a standard Linux workstation (128 Go RAM, 20 cores) with FEM ranges from 30 min to 10 h for the meshes with 0.96 and 5.02×10^6 elements, respectively, while it takes from 15 min to 14 h with FFT on the grids with 127^3 and 511^3 voxels. For the cases considered here, the computations times are then of comparable orders of magnitude.

3.2. Creep response

The macroscopic response in terms of axial creep strains averaged for the three realizations of the different aggregate shapes are summarized in Fig. 8 a). It can be classically observed that more regular and 'isotropic' shapes (the extreme case being spherical aggregates) provide lower "stiffness", the highest "stiffness" being those of the realistic microstructures generated with real aggregates exhibiting non-convex and flattened/elongated shapes with acute angles (referred to as "concrete" in all figures). The response of microstructures with "anisotropic Voronoi shapes" is then situated as expected between the "concrete" and the "isotropic Voronoi shapes" ones. Note that the curve of the "concrete" samples is very close to the one of the real sample obtained by tomography, which proves the suitability and accuracy of the reconstructed volumes from real aggregates. By contrast, the differences between the "concrete" and sphere samples curves are important, highlighting the

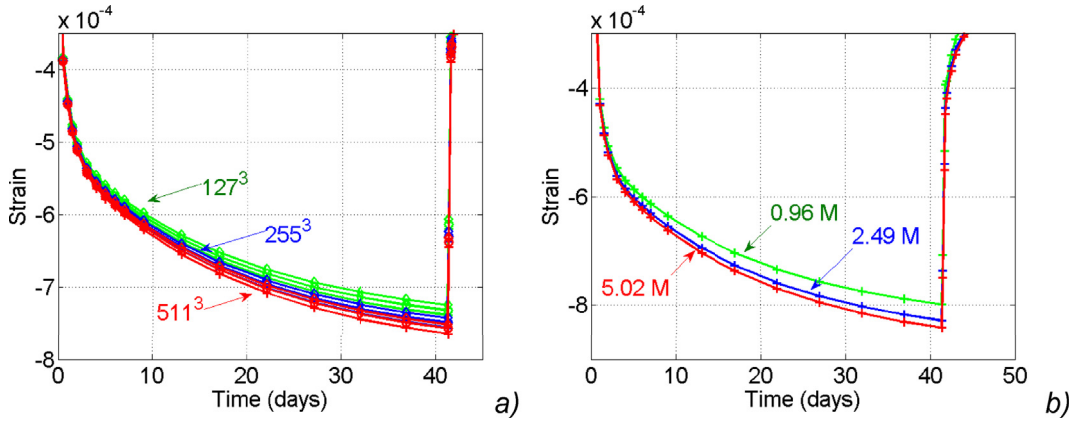

Fig. 7. a) Convergence of the axial creep response for three different refinement of the three realizations of the "virtual concrete" mesostructure in FFT and b) three Finite Element mesh refinements for an isotropic Voronoi microstructure.

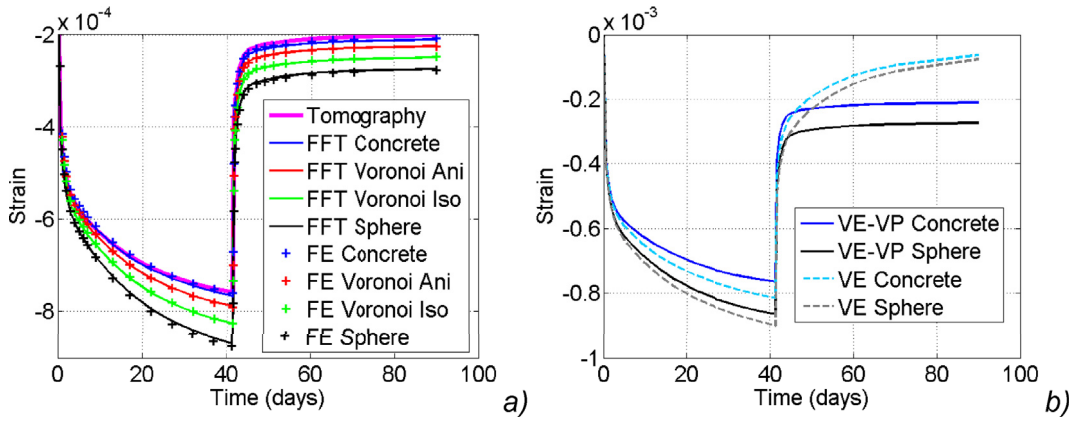

Fig. 8. a) Macroscopic axial strain for all the aggregate shapes with the VE-VP matrix model, and b) with the two models using spheres and "virtual concrete" mesostructures.

interest of accounting for precise aggregate shapes. It is worth mentioning that the "reinforcing" effect of non-convex flattened or acicular aggregate shapes is related to the stiffer behavior of the aggregates compared to the matrix. The aggregates would be softer than the matrix, the flattening effect would be to soften the overall material.

Following what was shown in the boundary condition study (Fig. 5), it can also be observed that FE computations using SUBC are in good agreement with FFT computations for all considered aggregate shapes. Another interesting feature is the very good agreement between the FFT direct computations on the aperiodic segmented tomography with the generated mesostructures that are truly periodic (blue and purple curves). This result demonstrates that edge effects due to the non-periodic mesostructure of real tomographic images are of minor importance as far as macroscopic behavior is concerned, and for the conditions (in particular phase contrasts) retained in this analysis.

Although identified on the same experimental data than the linear viscoelastic model and providing a near identical creep response (Fig. 1), the viscoelastic-viscoplastic model considered for the cementitious matrix is non-linear in particular due to the flow stress threshold that has been postulated; plasticity induces a modified stress redistribution between the matrix and aggregate phases relative to a linear viscoelastic matrix behavior. It can be seen in Fig. 8 b) than the macroscopic response is softer for a linear viscoelastic matrix than for the VE-VP material model for the two extreme aggregate shapes (similar results have been obtained with the other shapes but are not shown here for clarity reasons). The VE-VP model allows then the matrix to sustain comparable stress levels (see Fig. 9) with slightly lower strain magnitude than the purely VE approach. Obviously, the linear viscoelastic matrix provides a fully recoverable creep behavior.

Volume average axial stress evolutions in both matrix and aggregates phases are given in Fig. 9 a) during the creep phase. It can first be concluded that FFT and FE computations provide very similar results on this more local quantity. Besides, we observe that as expected the magnitude of the stress is much higher in the aggregate phase than in the matrix one, and that interestingly the effects of the irregularity in the aggregate shapes is to increase this magnitude difference: the axial stresses in matrix and aggregate phases are significantly closer for spherical shape than for real aggregate shapes. The curves for the different shapes are ordered as identified in Fig. 8 a) (i.e., the "sphere" curve is followed by the "isotropic Voronoi", then the "anisotropic Voronoi" and finally the "concrete" one). Another aspect is that after the first 3–4 days following the application of the creep loading, the average axial stress redistribution appears almost nonexistent in the case of the VE-VP behavior, while in the purely VE case a non-negligible evolution takes place, leading to a progressive increase in the stress magnitude difference between matrix and aggregate phases. In the recovery phase, some small discrepancy is noted between FE and FFT results although the ordering of the different responses is preserved. At unloading (see Fig. 9 b), a "jump"

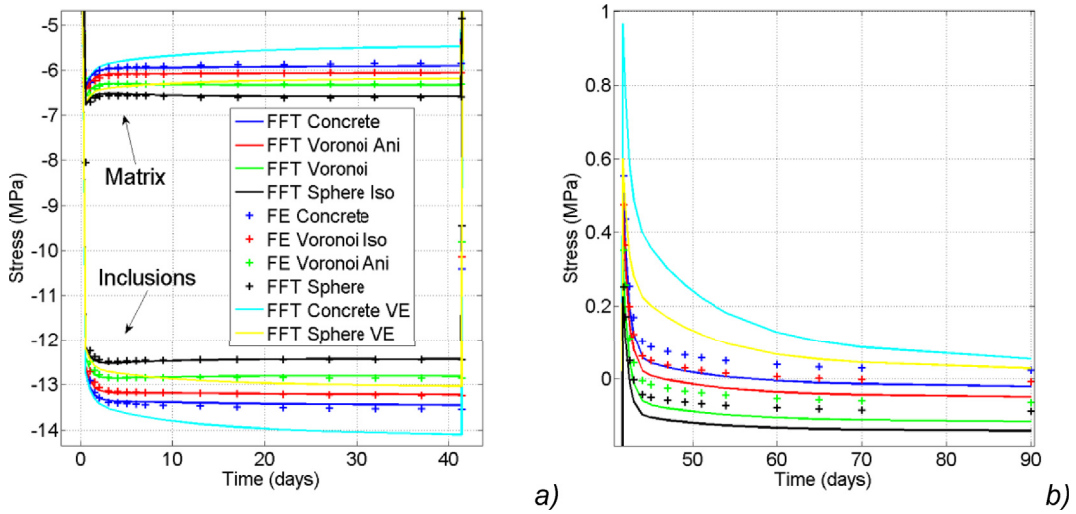

Fig. 9. a) Axial stress averages per phase for all the aggregate shapes (plus the matrix linear viscoelastic case for the "virtual concrete" and spherical shape) during the creep phase, b) matrix average axial stress in the recovery phase (same color code).

in tension is observed, due to the equilibrium occurring between the elastic aggregate phase and the matrix having stress-free accumulated creep strains. This tensile stress does not exceed 0.5 MPa and 1 MPa for VE-VP and purely VE behavior, respectively, and rapidly decreases especially in the VE-VP case.

Although there is necessarily zero residual stress at long-term for the linear viscoelastic matrix, it can be observed that viscoplasticity induces in most cases a small compressive residual average stress lower than −0.1 MPa in the matrix, though almost negligible for realistic aggregate shapes. Interestingly, this residual stress field of approximately zero average is highly heterogeneous and has a structure aligned with the loading direction (see Fig. 10 b) and d)), exhibiting tensile bands that may reach locally 1.5 MPa. We can observe that these tensile bands are located essentially between very close aggregates in the loading direction, while in the regions where matrix phase dominates, the axial residual stress become mostly negative. This straightforwardly results from the elastic behavior of the aggregates in a plastically deformed matrix. In can indeed be verified that the tensile residual stress zones (Fig. 10 b)) coincide with zones of higher cumulated plastic strains (Fig. 10 d)), in turn resulting from higher magnitude of total stresses (Fig. 10 c)). Clearly, as expected because of the stiffer behavior of aggregate phase, the effect of a greater proximity of aggregates in the compression loading direction is to increase and concentrate the compressive stresses in the matrix between aggregates. Note that these areas of tensile residual stress (corresponding to higher compression stress magnitude) may not necessarily be associated to areas of preferential damage.

Indeed in the case of compression loading the initiation and propagation of microcracking result mostly from tensile strains occurring perpendicular to the global compressive direction. The regions confined between close aggregates are not likely to be the best candidates for such perpendicular tensile strains (see e.g. Ref. [38]). This aspect would deserve further investigations and will be the objective of a subsequent specific study.

3.3. Local fields and damage index

As mentioned in the previous subsection, local stress and strain fields are of interest regarding the occurrence of damage, as could be taken into account using for example a Mazars law coupled to a creep model [39, 40]. Damage is not explicitly taken into account in the non-linear VE-VP model but some insight about damage mechanisms can be brought by the analysis of local fields.

Axial stress distributions per phase are plotted in Fig. 11 for several aggregate shapes at the end of the simulated creep phase from FFT results. The results obtained with a purely linear viscoelastic matrix (VE) for the “virtual concrete” are also reported. Note that in the case of FFT the distributions are straightforwardly calculated from the values per voxel, meaning these are volume-averaged quantities. It can be observed that local fields in the aggregate phase are highly dependent on the aggregate shape. Although aggregate volume distributions are identical, the complexity of aggregate shapes induces differences in term of dispersion of the stress fields. Irregular, non-convex and pointed shapes result in large spreading of aggregate stresses, as in the case of “virtual concrete” and anisotropic mesostructures, whose distributions appear very close. Interestingly, the axial stress dispersion in virtual concrete is also nearly the same for both VE-VP and VE models. By contrast, “isotropic Voronoi” and, above all, “sphere” aggregate shapes show a much narrower and quasi-symmetrical distribution, whose peak position is then in line with the aggregate phase mean value reported in Fig. 9 a) around −12.5 MPa. This is not the case for the “anisotropic Voronoi” and “concrete” distributions, which appear left-skewed with maximum value ranging between −11 and −10 MPa while the mean stress is calculated at

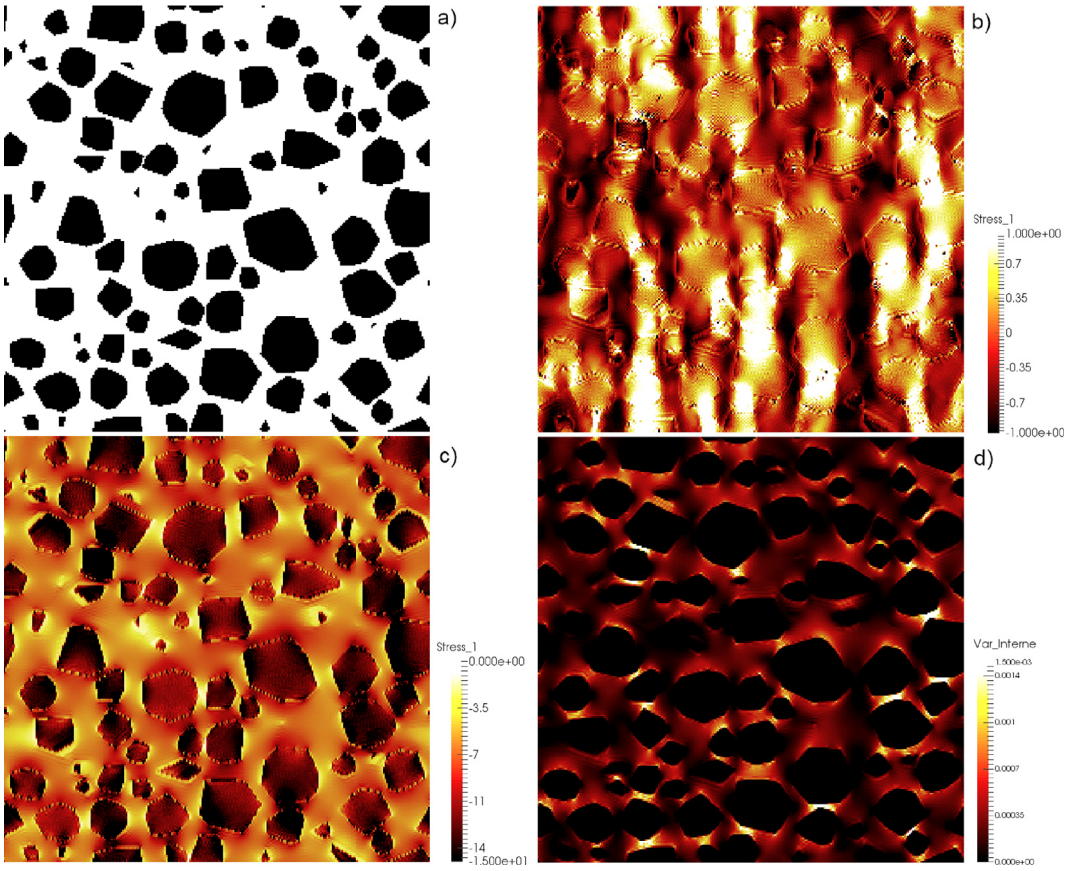

Fig. 10. Fields computed using FFT for a sample with isotropic Voronoi aggregates using the VE-VP model: a) Aggregates positions, b) residual axial stresses at t = 90 days (MPa), c) axial stresses at the end of the creep phase t = 42 days (MPa), d) cumulated plastic strain at t = 90 days. The loading direction is vertical.

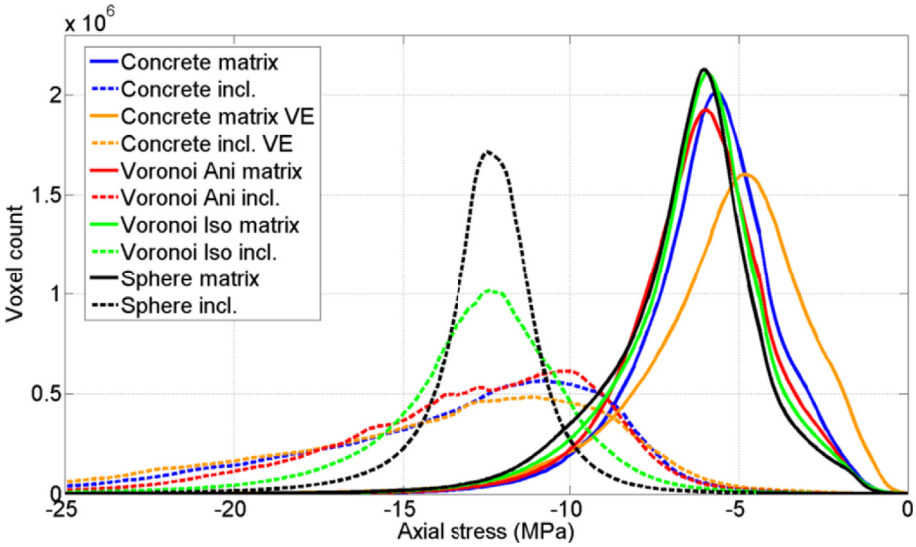

Fig. 11. Distribution of axial stresses obtained in aggregate and matrix phases with FFT for different shapes of aggregates at the end of the creep phase (42 days); the results obtained with a purely linear viscoelastic matrix (VE) for the "virtual concrete" are also reported.

about −13.5 MPa. This indicates that a non-negligible fraction of the aggregate phase sustains axial stresses significantly lower than this mean stress.

On the other hand, no substantial difference is observed regarding the matrix stress distributions using the VE-VP model, which appear relatively narrow with few skewness. The linear viscoelastic model (VE) shows however significantly different fields, with slightly more disperse matrix stresses. Differences are essentially coming from the non-linear nature (*i.e.,* presence of plastic strains) of the VE-VP model. It is worthwhile noting that in the VE-VP case, providing the hypotheses of a compression-induced microcracking initiation in the matrix phase together with the suitability of approaches based on micromechanics and stress fluctuations to estimate the compressive strength (see e.g. Refs. [41–43]), the influence of the aggregate shape seems to be weak on strength. Assuming a simplified spherical shape in such estimation models appears then justified.

Comparing the results between FFT and FE methods, we find that local fields agree relatively well as shown in Fig. 12, with the FFT distribution obtained directly from the voxel fields (as in Fig. 11) and FE one with the finite element field weighted by the element volume, even though the FFT and FE spatial discretization is significantly different. The FE stress distributions in the matrix phase appear however more largely spread out than the FFT ones; this may be explained by the finite element sizes that are generally noticeably higher than the FFT voxels, implying that one finite element provides less detailed information than one voxel. On this Figure step 2 and step 17 correspond to 1 day of loading and the end of the creep phase (42 days), respectively. The extent of stress redistribution during the creep phase from step 2 to step 17 between aggregate and matrix is also very small compared to viscoelasticity [40], as was already shown with stress averages in Fig. 9.

We now examine briefly the results in light of an index illustrating in a very simplified manner the cracking tendency. The widely used Mazars model makes use of an equivalent strain for the computation of the damage variable [44]. We assume that this equivalent strain can be used as a scalar indicator of the severity of the applied loading in the matrix, whose behavior is brittle with both tension and compression strength much lower than the aggregate one. It takes the following form:

$$\varepsilon_{Mazars} = \sqrt{\sum_i \varepsilon_i^2} \tag{9}$$

where the ε_i are the eigenvalues of the total strain tensor and ε_i their

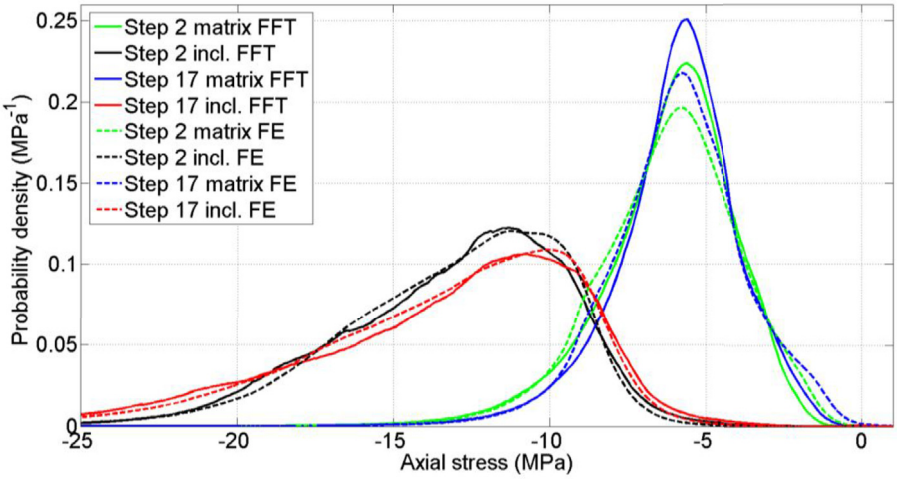

Fig. 12. Axial stress redistributions between the beginning (step 2) and the end of the creep phase (step 17) in the matrix and the aggregates for the virtual concrete, using FFT and FE methods.

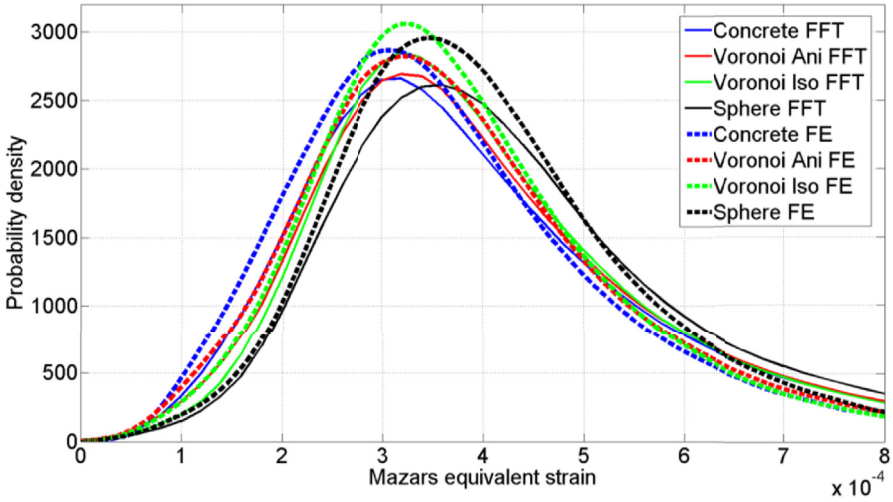

Fig. 13. Mazars equivalent strain distribution in the matrix for all the aggregate shapes at the end of the creep phase, for FE and FFT results.

positive part. Note that the classical value of equivalent strain used as threshold for damage initiation is around 10^{-4} for most concretes. This threshold value is closely related to the tensile strength, while in compression as considered in this study it is of less importance. The behavior in case of compressive states of stresses is much more ductile than in tension, and the damage propagation is then controlled by the (positive) extension strains perpendicular to the compression direction. Fig. 13 presents a comparison of the equivalent strain distributions in the matrix for the different mesostructure shapes computed using FE and FFT. The values used to compute this distribution are taken per voxel in the case of FFT calculation and per Gauss integration point in the FE case. It is important to notice that this equivalent strain cannot be rigorously related to damage since crack initiation and propagation is accompanied by substantial stress and strain redistributions, which are not taken into account in our modelling. Accordingly, the results should be validated against suitable experimental results of microcracking characterization.

Consistently with previous information on the strain fields, mesostructures with spherical aggregates seem to show slightly higher Mazars equivalent strains and could exhibit earlier damage compared to more irregular aggregate shapes, which may be seen as counterintuitive. It is therefore suspected that analytical estimates of mechanical properties obtained for elastic spherical aggregates in linear viscoelastic matrices would provide conservative evaluation of damage properties.

As this equivalent strain distribution is computed differently for FE and FFT solution fields, moderate differences in the results are obtained. Distributions are centered on the same values; differences are mostly expected in the properties of the long distribution tail that is however of importance since cracking will be initiated at these locations of higher strains. As already mentioned, more advanced simulations with an accurate description of fully matrix damage initiation and propagation (and associated stress-strain redistribution) would be necessary to evaluate if this difference is relevant. A regularization scheme for the used softening law would be however a prerequisite to ensure mesh independence.

4. Conclusions

In this paper, the creep response of numerically generated 3D concrete samples composed of a homogeneous viscoelastic matrix with randomly dispersed elastic aggregates of various size and shape has been investigated. The focus has been put on the effects of aggregate shapes (i.e., tomographic versus numerical convex aggregates) on both overall and local response, the influence of the creep model (linear viscoelastic versus viscoelastic-viscoplastic) and the impact of the numerical methods (FEM versus FFT-based method) for solving the problem. Specifically, the representativeness of the virtual samples and their corresponding aggregate shape is analyzed by comparing their response with the one of real concrete in terms of macroscopic strain, per phase average strain and stress evolutions, and stresses and strains distribution in both phases in the case of a creep loading followed by unloading. The important impact of the shape of aggregate has been highlighted and quantified on both macroscopic and microscopic results, justifying the interest to consider accurate and realistic shapes for more precise analyses. In particular and as expected, with respect to the real mesostructure, the more marked differences are reported with spherical aggregates, whereas the response of samples generated with tomographic aggregates is very close. The discrepancies with the concrete specimen increase with, in the order, flattened Voronoi aggregates, then isotropic ones. To sum up, numerical samples constructed with tomographic aggregates may be regarded as a very good approximation of real specimens, while more 'isotropic' and convex shapes lead to softer and softer behavior and exhibit noticeable macroscopic and local differences. This outcome regarding the influence of purely numerical convex aggregates is more significant than in Refs. [7,8], probably due to the more important phase contrast, to the different volume fractions considered and also to more angular shapes.

The results obtained with FEM and FFT method are very close when static uniform (SUBC) or periodic boundary conditions (PBC) are applied, even with a relatively limited mesh size (*i.e.*, the FE computation time with SUBC is equal to about 2 h, compared to the times presented in 3.1.2). This means that, though FFT is particularly well adapted for the proposed analysis, FEM remains in practice an interesting means to solve problems on representative material volumes, providing the meshes are carefully generated and of good quality. Regarding the response obtained with linear viscoelastic and viscoplastic models, important differences are reported as expected in the unloading stage due to the development of residual strains in the VP case. The non-negligible disparities in the creep stage are also attributed to this plastic strains development, which leads to a different repartition of strains and stresses in particular in the matrix phase. It has been observed that due to the stiffer behavior of aggregate phase, a lower distance between aggregates in the compression loading direction increases and concentrates the compressive stresses in the corresponding matrix region, leading to the development of plastic strains.

In the future, a damage model will be introduced in the matrix formulation to investigate the microcracking initiation and propagation in the mesoscopic samples subjected to various loadings, including thermal and hydric ones. As the interfaces (ITZ) between aggregates and mortar matrix have generally weaker mechanical properties than the matrix, they will also be considered in the modelling to describe a possible decohesion. In parallel, experiments based on Computed Tomography will allow accurately characterizing the microcracking development, and will serve to validate the models.

Acknowledgements

The authors would like to thank Dietmar Meinel from BAM for the X-CT images, EDF and the support from ANR MACENA project, and the following colleagues for the development and use of their software: Thomas Helfer (MFront), Lionel Gélébart (AMITEX_FFTP) and Christophe Bourcier (Combs).

References

[1] G. Li, Y. Zhao, S.-S. Pang, Four-phase sphere modeling of effective bulk modulus of concrete, Cement Concr. Res. 29 (6) (Jun. 1999) 839–845.
[2] G. Constantinides, F.J. Ulm, The effect of two types of CSH on the elasticity of cement-based materials: results from nanoindentation and micromechanical modeling, Cement Concr. Res. 34 (1) (2004) 67–80.
[3] M. Königsberger, B. Pichler, C. Hellmich, "Micromechanics of ITZ–aggregate interaction in concrete Part I: stress concentration, J. Am. Ceram. Soc. 97 (2) (2014) 535–542, https://doi.org/10.1111/jace.12591.
[4] C.F. Dunant, et al., A critical comparison of several numerical methods for computing effective properties of highly heterogeneous materials, Adv. Eng. Software 58 (April 2013) 1–12.
[5] I. Simonovski, L. Cizelj, Automatic parallel generation of finite element meshes for complex spatial structures, Comput. Mater. Sci. 50 (5) (Mar. 2011) 1606–1618.
[6] F. Bernard, S. Kamali-Bernard, Numerical study of ITZ contribution on mechanical behavior and diffusivity of mortars, Comput. Mater. Sci. 102 (May 2015) 250–257.
[7] F. Lavergne, K. Sab, J. Sanahuja, M. Bornert, C. Toulemonde, "Investigation of the effect of aggregates' morphology on concrete creep properties by numerical simulations, Cement Concr. Res. 71 (May 2015) 14–28.
[8] B. Bary, C. Bourcier, T. Helfer, Analytical and 3D numerical analysis of the thermoviscoelastic behavior of concrete-like materials including interfaces, Adv. Eng. Software 112 (2017) 16–30.
[9] A. Idiart, J. Bisschop, A. Caballero, P. Lura, A numerical and experimental study of aggregate-induced shrinkage cracking in cementitious composites, Cement Concr. Res. 42 (2) (février 2012) 272–281.
[10] A. Caballero, C.M. López, I. Carol, 3D meso-structural analysis of concrete specimens under uniaxial tension, Comput. Methods Appl. Mech. Eng. 195 (52) (Nov. 2006) 7182–7195.
[11] T. Wu, P. Wriggers, "Multiscale diffusion–thermal–mechanical cohesive zone model for concrete, Comput. Mech. (Apr. 2015) 1–18.
[12] J. Escoda, F. Willot, D. Jeulin, J. Sanahuja, C. Toulemonde, Estimation of local stresses and elastic properties of a mortar sample by FFT computation of fields on a 3D image, Cement Concr. Res. 41 (5) (May 2011) 542–556.
[13] Z. Yang, et al., In-situ X-ray computed tomography characterisation of 3D fracture evolution and image-based numerical homogenisation of concrete, Cement Concr. Compos. 75 (Jan. 2017) 74–83.
[14] B. Bary, C. Bourcier, T. Helfer, Thermoviscoelastic analysis of concrete creep at mesoscale, Key Eng. Mater. 711 (2016) 652–658.
[15] C. Mazzotti, M. Savoia, "Nonlinear creep, Poisson's ratio, and creep-damage interaction of concrete in compression, Mater. J. 99 (5) (Sep. 2002) 450–457.
[16] P. Rossi, J.-L. Tailhan, F. Le Maou, L. Gaillet, E. Martin, Basic creep behavior of concretes investigation of the physical mechanisms by using acoustic emission, Cement Concr. Res. 42 (1) (Jan. 2012) 61–73.
[17] T. You, R.K. Abu Al-Rub, M.K. Darabi, E.A. Masad, D.N. Little, "Three-dimensional microstructural modeling of asphalt concrete using a unified viscoelastic–viscoplastic–viscodamage model, Constr. Build. Mater. 28 (1) (Mar. 2012) 531–548.
[18] Z.P. Bazant, J.C. Chern, Concrete creep at variable humidity: constitutive law and mechanism, Mater. Struct. 18 (1) (1985) 1–20.
[19] Z. Bazant, A. Hauggaard, S. Baweja, F. Ulm, Microprestress-solidification theory for concrete creep 1. Aging and drying effects, J. Eng. Mech. 123 (11) (Nov. 1997) 1188–1194.
[20] M.K. Darabi, R.K. Abu Al-Rub, E.A. Masad, C.-W. Huang, D.N. Little, "A thermo-viscoelastic–viscoplastic–viscodamage constitutive model for asphaltic materials, Int. J. Solid Struct. 48 (1) (Jan. 2011) 191–207.
[21] R.A. Schapery, Nonlinear viscoelastic and viscoplastic constitutive equations with growing damage, Int. J. Fract. 97 (1–4) (Apr. 1999) 33–66.
[22] L.J. Parrott, Lateral strains in hardened cement paste under short- and log-term loading, Mag. Concr. Res. 26 (89) (1974).
[23] T. Crochon, T. Schönherr, C. Li, M. Lévesque, On finite-element implementation strategies of Schapery-type constitutive theories, Mech. Time-Dependent Mater. 14 (4) (May 2010) 359–387.
[24] T. Helfer, B. Michel, J.-M. Proix, M. Salvo, J. Sercombe, M. Casella, Introducing the open-source mfront code generator: application to mechanical behaviours and material knowledge management within the PLEIADES fuel element modelling platform, Comput. Math. Appl. 70 (5) (2015) 994–1023.
[25] H. Moulinec, P. Suquet, A numerical method for computing the overall response of nonlinear composites with complex microstructures, Comput. Methods Appl. Mech. Eng. 157 (1998) 69–94.
[26] L. Gélébart, R. Mondon-Cancel, Non-linear extension of FFT-based methods accelerated by conjugate gradients to evaluate the mechanical behavior of composite materials, Comput. Mater. Sci. 77 (Sep. 2013) 430–439.
[27] L. Gélébart, F. Ouaki, Filtering material properties to improve FFT-based methods for numerical homogenization, J. Comput. Phys. 294 (Aug. 2015) 90–95.
[28] Z. Qian, E.J. Garboczi, G. Ye, E. Schlangen, Anm: a geometrical model for the composite structure of mortar and concrete using real-shape particles, Mater. Struct. 49 (1–2) (Jan. 2016) 149–158.
[29] E.J. Garboczi, J.W. Bullard, 3D analytical mathematical models of random star-shape particles via a combination of X-ray computed microtomography and spherical harmonic analysis, Adv. Powder Technol. 28 (2) (2017) 325–339.
[30] C. Bourcier, W. Dridi, L. Chomat, E. Laucoin, B. Bary, E. Adam, Combs: Open Source python Library for RVE Generation. Application to Microscale Diffusion Simulations in Cementitious Materials, 2014, p. 2107.
[31] T. de Larrard, B. Bary, E. Adam, F. Kloss, Influence of aggregate shapes on drying and carbonation phenomena in 3D concrete numerical samples, Comput. Mater. Sci. 72 (2013) 1–14.
[32] T.T.H. Nguyen, B. Bary, T. de Larrard, Coupled carbonation-rust formation-damage modeling and simulation of steel corrosion in 3D mesoscale reinforced concrete, Cement Concr. Res. 74 (Aug. 2015) 95–107.
[33] E. Gilbert, D. Johnson, S. Keerthi, "A fast procedure for computing the distance between complex objects in three space," in *1987*, in: IEEE International Conference on Robotics and Automation Proceedings, vol. 4, 1987, pp. 1883–1889.
[34] S. Thomas, Y. Lu, E.J. Garboczi, Improved model for three-dimensional virtual concrete: anm model, J. Comput. Civ. Eng. 30 (2) (Mar. 2016) 4015027.
[35] T. Kanit, S. Forest, I. Galliet, V. Mounoury, D. Jeulin, Determination of the size of the representative volume element for random composites: statistical and numerical approach, Int. J. Solid Struct. 40 (13–14) (Jul. 2003) 3647–3679.
[36] M. Salmi, F. Auslender, M. Bornert, M. Fogli, Apparent and effective mechanical properties of linear matrix-inclusion random composites: improved bounds for the effective behavior, Int. J. Solid Struct. 49 (10) (mai 2012) 1195–1211.
[37] S. Pecullan, L.V. Gibiansky, S. Torquato, Scale effects on the elastic behavior of periodic and hierarchical two-dimensional composites, J. Mech. Phys. Solid. 47 (7) (juin 1999) 1509–1542.
[38] Y. Huang, Z. Yang, W. Ren, G. Liu, C. Zhang, 3D meso-scale fracture modelling and validation of concrete based on in-situ X-ray Computed Tomography images using damage plasticity model, Int. J. Solid Struct. 67 (68) (Aug. 2015) 340–352.
[39] C. Mazzotti, M. Savoia, Nonlinear creep damage model for concrete under uniaxial compression, J. Eng. Mech. ASCE 129 (9) (Sep. 2003) 1065–1075.
[40] M.-Q. Thai, B. Bary, Q.-C. He, A homogenization-enriched viscodamage model for cement-based material creep, Eng. Fract. Mech. 126 (Aug. 2014) 54–72.
[41] B. Pichler, C. Hellmich, Upscaling quasi-brittle strength of cement paste and mortar: a multi-scale engineering mechanics model, Cement Concr. Res. 41 (5) (2011) 467–476.
[42] F. Lavergne, A. Ben Fraj, I. Bayane, J.F. Barthélémy, Estimating the mechanical properties of hydrating blended cementitious materials: an investigation based on micromechanics, Cement Concr. Res. 104 (Feb. 2018) 37–60.
[43] T. Honorio, L. Brochard, B. Bary, Statistical variability of mechanical fields in thermo-poro-elasticity: multiscale analytical estimations applied to cement-based materials at early-age, Cement Concr. Res. 110 (Aug. 2018) 24–41.
[44] J. Mazars, A description of micro-and macroscale damage of concrete structures, Eng. Fract. Mech. 25 (5–6) (1986) 729–737.